Highly Porous Ti_4O_7 Reactive Electrochemical Water Filtration Membranes Fabricated via Electrospinning/Electrospraying

Melissa C. Santos and Yossef A. Elabd
Dept. of Chemical Engineering, Texas A&M University, College Station, TX 77843

Yin Jing and Brian P. Chaplin
Dept. of Chemical Engineering, University of Illinois at Chicago, IL 60607

Lei Fang
Dept. of Chemical Engineering, University of Illinois at Chicago, IL 60607

College of Civil Engineering and Architecture, Zhejiang University, Hangzhou 310058, P.R. China

DOI 10.1002/aic.15093
Published online November 24, 2015 in Wiley Online Library (wileyonlinelibrary.com)

Porous, flexible, reactive electrochemical membranes (REMs) for water purification were synthesized by a novel simultaneous electrospinning/electrospraying (E/E) technique, which produced a network of poly(sulfone) fibers and Ti_4O_7 particles as evidenced by scanning electron microscopy. Cyclic voltammetry indicated that the kinetics for water electrolysis reactions and the $Fe(CN)_6^{4-/3-}$ redox couple were enhanced by Ti_4O_7 deposition using the E/E technique. Membrane filtration experiments using phenol as a model contaminant showed a 2.6-fold enhancement in the observed first-order rate constant for phenol oxidation ($k_{obs,phenol}$) in filtration mode relative to cross-flow operation. Phenol oxidation in filtration mode was approaching the pore diffusion mass transfer limit, and was 6 to 8 times higher than measured in a previous study that utilized a ceramic Ti_4O_7 REM operated in filtration mode and is comparable to rate constants obtained with carbon nanotube flow-through reactors, which are among the highest reported in the literature to date. © 2015 American Institute of Chemical Engineers *AIChE J*, 62: 508–524, 2016
Keywords: electrochemistry, environmental engineering, membrane materials, separation techniques

Introduction

Effective water treatment technologies need to treat a broad range of water contaminants, which typically is accomplished using multiple technologies in a treatment train. To reduce the cost and complexity of water treatment, research has focused on the development of novel technologies that can incorporate multiple treatment methods into a single technology. Recent work has focused on the integration of membrane filtration with electrochemical advanced oxidation processes to create a hybrid technology known as reactive electrochemical membranes (REMs).[1,2] This novel REM technology utilizes a ceramic porous substoichiometric Ti_nO_{2n-1} $(4 < n < 6)$ material (known as Magnéli phases) that can serve as both a membrane for filtration and a reactive electrode surface that can oxidize contaminants by a combination of hydroxyl radical ($OH^{\bullet}$) production from water oxidation and direct electron transfer reactions.[1,2]

The REMs are synthesized by the conversion of nonconductive TiO_2 precursors to conductive Magnéli phases, where Ti_4O_7 is the most electrically conductive phase. Due to their stability under anodic polarization and resistant to oxidation and corrosion,[3–6] conductive Ti_4O_7 electrodes have been utilized for the cathodic protection of metal structures[3] and electrodes for a variety of applications, including lead-acid batteries,[7,8] rechargeable zinc-air batteries,[5,6] and fuel cells.[4,9–11]

While only few studies have reported on the use of Ti_4O_7 for water purification,[1,2,12–17] Zaky and Chaplin[1,2] have expanded the use of Ti_4O_7 for water treatment by utilizing it as a REM to study the removal of a series of *p*-substituted phenolic compounds that were used as model organic contaminants. In their studies, they demonstrated that the REM was active for both direct anodic oxidation and generation of $OH^{\bullet}$ that resulted in efficient removal of phenolic compounds.[1,2] Although the porous rigid cylindrical REM used in these studies was effective, it had a limited morphology (e.g., limited porosity, geometry, flexibility) for filtration experiments. To expand the potential applications of REMs for water treatment, it is desirable to develop flexible REMs with tailored porosities that will facilitate the development of new hybrid membranes for use in compact filtration systems (e.g., spiral wound membrane modules and point-of-use devices).

Toward this goal, a simultaneous electrospinning and electrospraying method was pursued to develop Ti_4O_7 REMs that are highly porous, flexible, durable, and inexpensive. Simultaneous electrospinning and electrospraying is a recent method that can fabricate highly porous membranes by electrospinning

Correspondence concerning this article should be addressed to B. P. Chaplin at chaplin@uic.edu or Y. A. Elabd at elabd@tamu.edu.

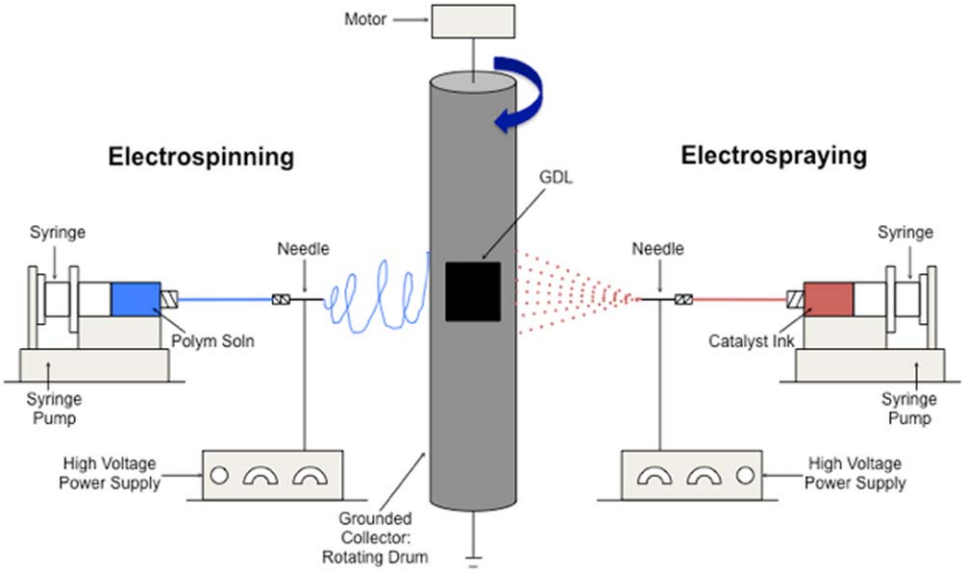

Figure 1. Schematic of simultaneous electrospinning/electrospraying (E/E) apparatus.[18]

[Color figure can be viewed in the online issue, which is available at wileyonlinelibrary.com.]

organic polymer nanofibers and electrospraying inorganic nanoparticles in tandem from two separate needles (see Figure 1). The resulting membranes produced from this method result in a network of nanofibers and nanoparticles with intimate contact between both materials throughout the porous matrix, where changing the various electrospinning and electrospraying parameters and solution properties allows for membranes with various porosities, fiber sizes, and particle sizes. Membranes fabricated from the electrospinning/electrospraying (E/E) method have recently been explored in a variety of applications, including batteries,[19] tissue engineering,[20–25] fuel cells,[18,26] composites,[27–29] and water purification.[28,30–32] To date, few studies have explored the E/E method to develop membranes for water purification and to our knowledge studies have not been conducted that have utilized the E/E method to develop REMs.

In this study, the simultaneous E/E method was employed to fabricate highly porous REMs consisting of poly(sulfone) (PSU) fibers and Ti_4O_7 particles using the two needle system shown in Figure 1. PSU is a commonly used polymer in filtration membranes[32–35] and Ti_4O_7 has previously been used for REMs due to its high conductivity and corrosion resistant properties.[3,5,6] Characterization of the E/E REMs was performed using x-ray diffraction (XRD), scanning electron microscopy (SEM), and Hg porosimetry analysis. The electrochemical properties and water filtration performance of these E/E REMs were evaluated using electrical impedance spectroscopy (EIS), cyclic voltammetry (CV), and cross-flow filtration experiments.

Experimental

Materials

TiO_2 (99.9%, 32 nm particles) nanopowder was purchased from Alfa Aesar. Ethanol (EtOH) (≥99.997%, anhydrous),-PSU (average $M_n \sim 22{,}000$ g/mol, beads), and dichloromethane (DCM) (≥99.8%, anhydrous) were purchased from Sigma Aldrich. High purity H_2 gas was purchased from Airgas and was used for Ti_4O_7 powder synthesis. Carbon cloth gas diffusion layers (GDL; ELAT LT 1400W and ELAT H) were purchased from Fuel Cells Etc. and were used as received for membrane fabrication. All other chemicals were reagent-grade and obtained from Sigma-Aldrich or Fisher and were used as received. All solutions used in this study were made using deionized water obtained from a NANOPure water purification system (Barnstead) with resistivity greater than 18 MΩ·cm (25°C).

Ti_4O_7 synthesis and structural characterization

Ti_4O_7 powder was prepared by reducing TiO_2 nanopowder in H_2 gas at 950°C in a tube furnace (Mode F21135, Barnstead Thermolyne) for 4 h.[6] The chemical reaction for the production of Ti_4O_7 is given[3]

$$4TiO_2 + H_2 \rightarrow Ti_4O_7 + H_2O \quad (1)$$

XRD (Bruker-D8 Advanced, Bragg Bentano) powder experiments were performed to quantify and characterize the Ti_4O_7 Magnéli phase. XRD patterns were collected from 15° to 70° 2θ with a scan rate of 0.3°/s. SEM (FEI Quanta 600 FE-SEM) was used to characterize the morphology of the Ti_4O_7 powder. Samples were sputter coated (Cressington 208 HR) with platinum at 40 mV to achieve a 6 nm layer thickness before SEM images were collected. SEM images of the Ti_4O_7 powder were collected at 10 kV.

Simultaneous E/E system

A schematic of the simultaneous E/E apparatus used is shown in Figure 1.[18] The apparatus consists of two high-voltage sources (Model PS/EL50R00.8, Glassman High Voltage and Model ES40P-10W/DAM, Gamma High Voltage Research), two syringe pumps (Model NE-1000, New Era Pump Systems), tubing (EW-30600-65, Cole Parmer and Pt. No. 86510, Hamilton), luer lock needle adaptors (Pt. No. 86511, Hamilton), two syringe needles (i.d. = 0.061 cm, Pt. No. 90520, Hamilton), two syringes (CG-3070-03, Chemglass Life Sciences), and a grounded collector consisting of an aluminum foil covered cylindrical drum connected to a motor (Model 4IK25GN-SW2, Oriental Motor). The motor allows for drum (o.d. = 4.85 cm) rotation during E/E experiments and was set at 100 rpm. GDLs were cut into 5 cm × 5 cm pieces,

Table 1. Summary of Membranes Fabricated

Sample Name	Membrane
ELAT 1	Bare ELAT 1 (ELAT LT 1400 W)
E/E-ELAT 1	E/E PSU/Ti_4O_7 on ELAT 1
E/E-ELAT 1-A	E/E PSU/Ti_4O_7 on ELAT 1 – post-annealed at 200°C for 2 h
SC-ELAT 1	Solution Cast PSU/Ti_4O_7 on ELAT 1
SC-ELAT 1-A	Solution Cast PSU/Ti_4O_7 on ELAT 1 – post-annealed at 200°C for 2 h
ELAT 2	Bare ELAT 2 (ELAT H)
E/E-ELAT 2	E/E PSU/Ti_4O_7 on ELAT 2
E/E-ELAT 2-A	E/E PSU/Ti_4O_7 on ELAT 2 – post-annealed at 200°C for 2 h
E/E-ELAT 2-A-2[a]	E/E PSU/Ti_4O_7 on ELAT 2 – post-annealed at 200°C for 2 h
SC-ELAT 2	Solution Cast PSU/Ti_4O_7 on ELAT 1
SC-ELAT 2-A	Solution Cast PSU/Ti_4O_7 on ELAT 1 – post-annealed at 200°C for 2 h

[a]E/E 2 day process time; all other E/E membranes 6 h process time.

and four GDL pieces were adhered onto the drum for each E/E experiment. E/E experiments consisted of simultaneously electrospinning a PSU/DCM solution and electrospraying a Ti_4O_7/EtOH solution. For the electrospinning process, the needle tip to collector distance, applied voltage, and solution flow rates were 12 cm, 12 kV, and 0.9 mL/h, respectively. For the electrospraying process, the needle tip to collector distance, applied voltage, and solution flow rates were 9 cm, 15 kV, and 3 mL/h, respectively.

Membrane fabrication

PSU solutions for electrospinning were prepared by dissolving 1 g of PSU in 10 g of DCM to produce a 9.1 wt % PSU/DCM solution. The polymer solutions were mixed for 24 h to ensure homogeneity. The Ti_4O_7 solutions for electrospraying were prepared by dissolving 0.25 g of Ti_4O_7 powder in 9.75 g of EtOH to produce a 2.5 wt % Ti_4O_7/EtOH solution. The Ti_4O_7 solution was then sonicated for 15 min (Model Cl-18, QSonica Sonicator). The Ti_4O_7 and PSU solutions were used for E/E experiments. E/E experiments were conducted over the course of 6 h using either the ELAT LT1400W or the ELAT H GDLs as a substrate collector on the drum. ELAT LT1400W and ELAT H are woven carbon cloth membranes. The ELAT LT 1400W GDL has a thickness of 454 μm, 63% porosity, is poly(tetrafluoroethylene) (PTFE) treated and has a microporous carbon layer covering the woven carbon cloth. The ELAT H GDL has a thickness of 406 μm, 80% porosity, is not PTFE treated, and does not have a microporous carbon layer covering the woven carbon cloth. The ELAT LT 1400W and ELAT H GDLs were used because they provided structural support for the E/E and solution cast PSU/Ti_4O_7 membranes, and were durable, flexible, and highly conductive. In this study, the ELAT LT 1400W and ELAT H GDLs will be referred to as ELAT 1 and ELAT 2, respectively. E/E experiments were also conducted over the course of 2 days using the ELAT H GDL (ELAT 2) to compare to the shorter 6 h deposition E/E membranes. Several of the E/E membranes were annealed at 200°C for 2 h to investigate the impact of annealing. The resulting filtration membranes consisted of GDL coated with a layer of electrospun PSU nanofibers and electrosprayed Ti_4O_7 particles. These materials will be referred to as E/E membranes.

As a comparative control sample, PSU/Ti_4O_7 solutions were cast onto GDLs. The PSU/Ti_4O_7 solution used to create these solution cast membranes were prepared by dissolving 1 g of PSU in 10 g of DCM for 24 h to produce a 9.1 wt % PSU/DCM solution. The solution was mixed for 24 h to ensure homogeneity. Then 0.25 g of Ti_4O_7 was added to the solution and mixed for 24 h to ensure complete mixing. This solution concentration resulted in solution cast membranes with the same amount of Ti_4O_7 as the E/E membranes. This solution was then cast onto 5 cm $\times$ 5 cm pieces of both the ELAT 1 and ELAT 2 GDLs. The solution cast membranes were allowed to dry in a fume hood for 24 h, and then were annealed at 200°C for 2 h. The resulting filtration membranes consisted of GDL coated with a layer of solution cast PSU/Ti_4O_7. These will be referred to as solution cast membranes. Table 1 summarizes all of the membranes fabricated in this study with an abbreviated sample name for each, which will be used throughout the manuscript from this point forward.

Membrane characterization

SEM (FEI Quanta 600 FE-SEM) was used for morphological characterization of the E/E and solution cast membranes before and after they were annealed. Samples were sputter coated (Cressington 208 HR) with platinum at 40 mV to achieve a 6 nm layer thickness before SEM images were collected. SEM images of the membranes were collected at 10 kV and a working distance of 10 mm. Additionally, E/E experiments were conducted over the course of 3 days on bare aluminum foil to create 1.17 g of free standing E/E membrane for Hg intrusion porosimetry analysis. Hg porosimetry analysis was also performed for ELAT 2, E/E ELAT 2-A, and E/E-ELAT 2-A-2. Hg intrusion porosimetry analysis was performed by Micromeritic Analytical Services (Norcross, GA).

The conductivities of each of the E/E membranes and solution cast membranes (control), and bare GDLs (control) were measured with EIS (Solartron, 1260 impedance analyzer, 1287 electrochemical interface, Z Plot software). The in-plane conductivities were measured using a cell with four parallel electrodes. An alternating current was applied to the two outer electrodes while the resistance, R, was measured between the two inner electrodes. Conductivities of each membrane were measured over a frequency range of 0.1 Hz to 10^6 Hz with amplitude of 1 mV in the sinusoidal perturbation. The real impedance or resistance was determined from the high x-intercept of a semicircle regression of the Nyquist plot data. The conductivity was calculated using the following equation

$$\sigma = \frac{L}{AR} \tag{2}$$

where σ is the conductivity, L is the length between the two inner electrodes, R is the resistance, and A is the cross-sectional area of the membrane ($A = wl$, where w is the width of the membrane and l is the thickness of the membrane). The conductivity of each membrane and GDL (ELAT 1 and ELAT 2) was measured six times and the conductivity and error reported is an average and standard deviation of these values.

Electrochemical characterization

The electrochemical characterization consisted of CV and EIS and was carried out in a single compartment three-electrode glass cell using a potentiostat (Interface 1000, Gamry). The ELAT sample was used as the working electrode and immersed in 100 mM $NaClO_4$ supporting electrolyte. Electrical contact was made using copper tape (Fisher). A platinum wire (Alfa Aesar, Ward Hill, MA) was used as counter electrode and a saturated Ag/AgCl electrode (Pine Instrument,

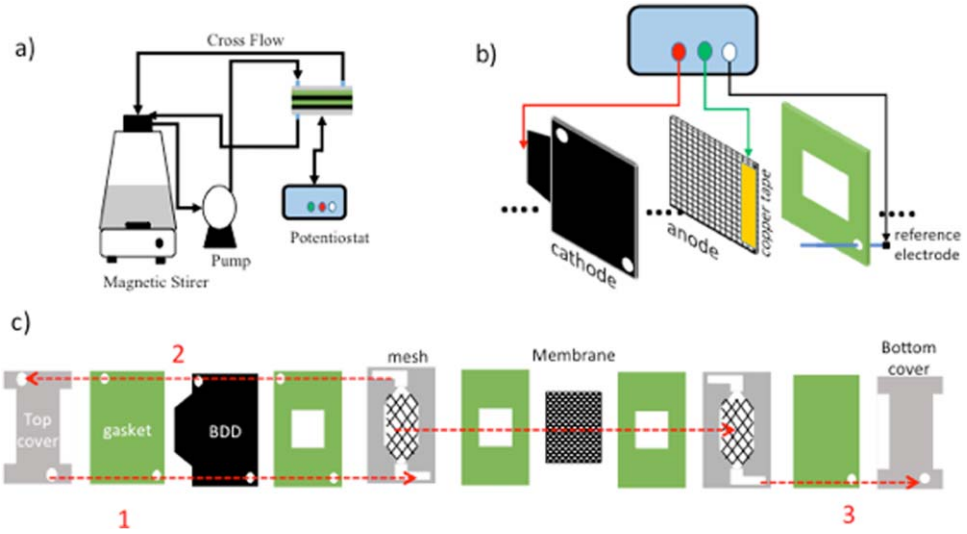

Figure 2. (a) Schematic of the membrane filtration setup, (b) electrical connection in the three-electrode setup, (c) components of the flow cell in exploded view.

Lines 1, 2, and 3 represent feed, retentate, and permeate streams, respectively. [Color figure can be viewed in the online issue, which is available at wileyonlinelibrary.com.]

PA) was used as a reference electrode. The reference electrode was placed 1 mm away from the ELAT surface to reduce solution resistance and all potentials were corrected for solution resistance (measured by EIS) and are reported against the standard hydrogen electrode (SHE). CV was conducted in both the supporting electrolyte and in supporting electrolyte containing both 5 mM $K_3Fe(CN)_6$ and 5 mM $K_4Fe(CN)_6$ at a scan rate of 50 mV s^{-1}.

The measurement of the double layer capacitance (C_{dl}) of select ELAT samples was made within the potential region between hydrogen and oxygen evolution reactions (0.2 to 0.6 vs. SHE), and at the scan rates of 2, 4, 8, and 10 mV s^{-1} in 100 mM $NaClO_4$ supporting electrolyte. In the C_{dl} measurement, an ELAT sample with a geometric surface area of 10 cm^2 was used as the working electrode, titanium mesh as counter electrode, and saturated Ag/AgCl as reference electrode. The capacitive current increases linearly with increasing scan rates so that the capacitance of each ELAT sample can be extracted from the slope of the charging current ($i_{charging}$) vs. scan rate (v) as given in Eq. 3

$$C_{dl} = \frac{i_{charging}}{v} \tag{3}$$

EIS experiments were conducted at the open circuit potential (OCP) in a quiescent solution containing 5 mM $K_3Fe(CN)_6$ and 5 mM $K_4Fe(CN)_6$ with an amplitude of 10 mV in the sinusoid perturbation and over a frequency range of 10 mHz to 30 kHz. The validity of the EIS data was examined by Kramers–Kronig relations. An equivalent circuit model consisting of a Randles circuit with Warburg impedance was fit to EIS data, and details of the model are discussed in the Results and Discussion Section. Fitting of the Randles circuit and examination of the Kramers–Kronig relation to EIS data were performed in Gamry Echem Analyst software (version 6.23). The simplex algorithm was used to minimize the sum of squared errors between experimental and simulated data. The fitting results are reported along with error estimates at 95% confidence intervals assuming a Chi-squared distribution.

Membrane filtration experiments

The cross-flow membrane filtration experimental setup is shown in Figure 2a. The feed solution consisted of 100 mM K_2HPO_4 as background electrolyte (pH = 4.5) and 1 mM phenol as target reactant. The background electrolyte concentration was chosen to mimic the ionic strength of industrial wastewater streams and reverse osmosis concentrates.[36–38] Phenol was chosen because is reacts *via* both direct oxidation and $OH^{\bullet}$ oxidation ($k_{phenol,OH^{\bullet}} = 6.6 \times 10^9$ M^{-1} s^{-1}).[39] A total volume of 300 mL feed solution was continuously stirred in the feed tank and was pumped past the membrane at a constant cross-flow rate ($Q_{cross} = 25.8$ L h^{-1}), using a bench analog drive gear pump (Cole Parmer). Two different flow configurations were tested: (1) cross-flow mode, where the REMs were placed on a stainless steel current collector and, thus, prevented liquid flow through the REM pores, and (2) filtration mode, where the REMs were placed on a 0.2 μm pore size polysulfone membrane support and liquid flow permeated through the membrane at a constant flux of $Q_{perm} = 6.1$ L h^{-1}, which corresponds to a normalized membrane flux of J = 6100 L m^{-2} h^{-1} (1.7×10^{-3} m s^{-1}). For both flow configurations, $Q_{cross} = 25.8$ L h^{-1}, the transmembrane pressure was ~14 kPa, and solutions were 100% recycled to the feed reservoir to characterize reaction kinetics. Constant current was supplied to the flow cell by a potentiostat with REM as anode and boron-doped diamond (BDD) plate as cathode. The electrode setup is shown in Figure 2b, and the flow cell assembly is shown in Figure 2c. The anode and cathode were 6 mm apart. The membrane was mounted between two gaskets with an exposed surface area of 10 cm^2 at the center. The electrical contact between membrane and the potentiostat was made using copper tape.

Prior to each experiment, a membrane was mounted into the flow cell and 2 L deionized water was pumped through the system in a nonrecycle mode. During 3 h of electrolysis, samples were taken from the feed tank every 20 min, filtered through a 0.45 μm PVDF filters and analyzed in HPLC (LC-20AD Shimadzu). HPLC analysis employed a SPD-M30A

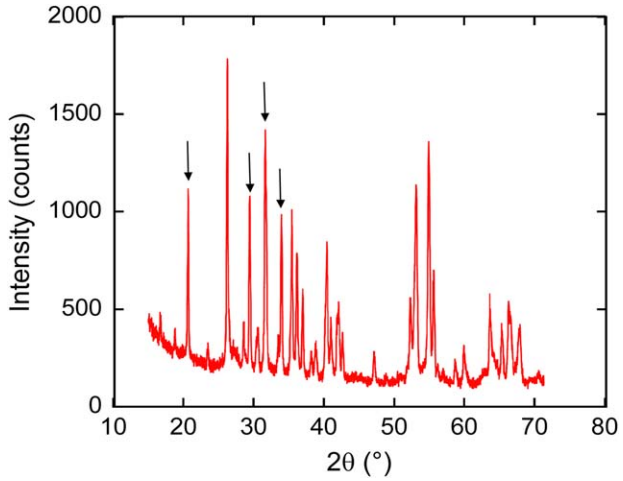

Figure 3. XRD pattern of synthesized Ti_4O_7 powder.

Characteristic Ti_4O_7 peaks indicated by arrows. [Color figure can be viewed in the online issue, which is available at wileyonlinelibrary.com.]

variable wavelength UV-Visible detector set at 254 nm and a reverse-phase C18 column (Phenomenex, 4.6 × 250 mm, 5 μm). Methanol:water (50:50, v/v) was used as mobile phase at the total flow rate of 1 mL·min^{-1}. The injection volume was programmed at 5 μL. Analysis was performed in duplicate and evaluated using LabSolutions Lite Version 5.63 software. After each experiment, solutions were pumped through the system in the following sequence: 2 L deionized water (nonrecycle), 200 mL 100% ethanol (recycle, 15 min), and 2 L deionized water (nonrecycle) to remove adsorbed contaminants. All experiments were performed in duplicate, that is, experiments were performed on multiple samples of each membrane.

Results and Discussion

Ti_4O_7 powder structure and morphological characterization

To fabricate E/E membranes with Ti_4O_7 particles, Ti_4O_7 powder was first synthesized by reducing TiO_2 nanopowder in hydrogen at 950°C for 4 h. After reduction in H_2, the resulting powder transitioned from a white color to a dark blue/black color. The Ti_4O_7 Magnéli phase present in the reduced TiO_2 nanopowder was confirmed by XRD. Figure 3 shows an XRD pattern of Ti_4O_7 powder used for creating E/E and solution cast membranes. The main peaks of interest for characterizing the Ti_4O_7 Magnéli phase occur at 20.7°, 29.6°, 31.7°, and 34.1°.[3,40] All of these peaks are present in the XRD pattern shown in Figure 3, confirming the presence of the Ti_4O_7 Magnéli phase in the reduced powder, and subsequently successful synthesis of Ti_4O_7 powder for E/E and solution cast membrane fabrication.

Since the reduction of TiO_2 powder typically produces a sample with at least two or more Magnéli phases, the XRD pattern shown in Figure 3 can be used to quantitatively determine the percentage of Ti_4O_7 in the reduced powder. Reduced TiO_2 powder contains more than one phase because as the reduction of TiO_2 powder proceeds, the powder undergoes successive reduction into several different Magnéli phases, and eventually Ti_4O_7 powder is produced. The other phase most commonly present in these samples is the Ti_5O_9 Magnéli phase. Goldschmidt and Watanabe determined the molecular fraction, N, of Ti_4O_7 in a sample by calculating the integrated intensity ratio of the corresponding peak of the Ti_4O_7 and Ti_5O_9 Magnéli phases for a specific plane.[40] The integrated intensity ratios were calculated for the 101 and 121 planes. The corresponding peaks for the 101 and 121 phases in Ti_4O_7 were 20.7° and 29.6°, respectively, and for Ti_5O_9 were 21.9° and 29.1°, respectively.[40] The integrated intensity ratio of each characteristic peak for a specific plane for both the Ti_4O_7 and Ti_5O_9 Magnéli phases can be represented as follows[40]

$$\frac{N_{59}}{N_{47}} = \frac{P'_{59}\upsilon_{59}F_{47}^2 LP(\theta_{47})}{P'_{47}\upsilon_{47}F_{59}^2 LP(\theta_{59})} \tag{4}$$

where N_{59} and N_{47} are the molecular fractions of Ti_5O_9 and Ti_4O_7, respectively, P'_{59} and P'_{47} are the integrated intensities of the corresponding peaks for one of the phases present in Ti_5O_9 and Ti_4O_7, respectively, v_{59} and v_{47} are the unit-cell volumes for Ti_5O_9 and Ti_4O_7, respectively, F_{59}^2 and F_{47}^2 are the triclinic structure factors for Ti_5O_9 and Ti_4O_7, respectively, and LP is the Lorentz-polarization factor. The expression for the Lorentz-polarization factor can be represented as follows[40]

$$\mathrm{LP}(\theta) = \frac{1+\cos^2(2\theta)}{\sin(2\theta)\sin(\theta)} \tag{5}$$

where 2θ is the angle for the corresponding peak for the plane of interest. Values for v_{59}, v_{47}, F_{59}^2, and F_{47}^2 were determined

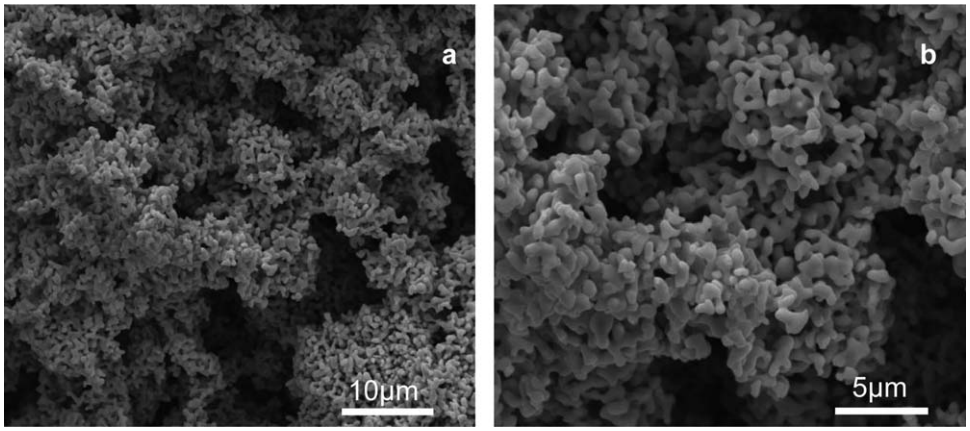

Figure 4. SEM images of Ti_4O_7 powder at (a) 5k X and (b) 10k X magnification.

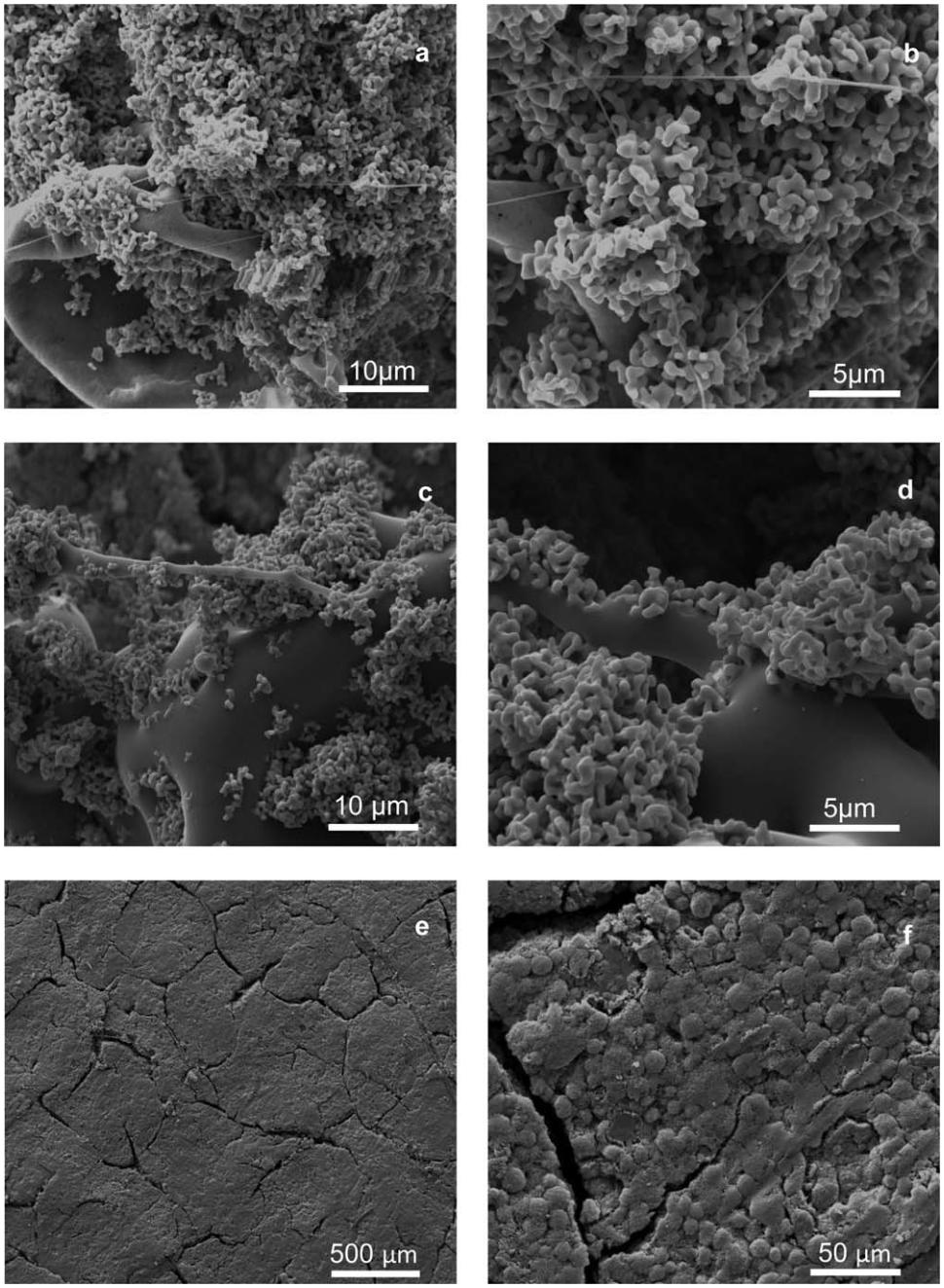

Figure 5. SEM images of E/E-ELAT 1 at (a) 5k X and (b) 10k X magnification and E/E-ELAT 1-A at (c) 5k X and (d) 10k X magnification and ELAT 1 at (e) 100 X and (f) 1k X magnification.

based on work done by LePage and Strobel;[41] v_{59} and v_{47} were 590 Å and 465 Å, respectively, and F^2_{59} were 5240 and 12070 and F^2_{47} were 3240 and 6990 for the 101 and 121 phases, respectively.[42] Using Eqs. 4 and 5, the molecular fractions of Ti_4O_7 and Ti_5O_9 were calculated in each sample of reduced TiO_2 powder produced. For the XRD pattern shown in Figure 3, the molecular fraction of Ti_4O_7 calculated in the powder was 94.3% ± 4.6%. On average, the Ti_4O_7 was 90.6% ± 4.6% for all the samples produced in this study.

The morphology of the Ti_4O_7 powder produced in this study was examined using SEM, and the images are shown in Figure 4. Figure 4a shows an SEM image of the Ti_4O_7 powder used to create the E/E and solution cast membranes. Figure 4b shows a magnified view of Figure 4a. Figure 4 shows that the Ti_4O_7 powder is highly aggregated, and the particles are neither spherical nor oblong shaped. Furthermore, unlike their precursor, TiO_2 nanopowder, Figure 4b shows that the Ti_4O_7 powder particle size is much larger due to the sintering process.

E/E membrane characterization

Morphological characterization of the E/E membranes was also performed using SEM. Figures 5a, b show SEM images of E/E membranes of electrospun PSU and electrosprayed Ti_4O_7 on ELAT 1 before the membranes were annealed (E/E-ELAT 1). Figure 5a shows PSU nanofibers and Ti_4O_7 particles. Figure 5b shows a magnified view of Figure 5a, where both Ti_4O_7 particles and PSU nanofibers can be seen more

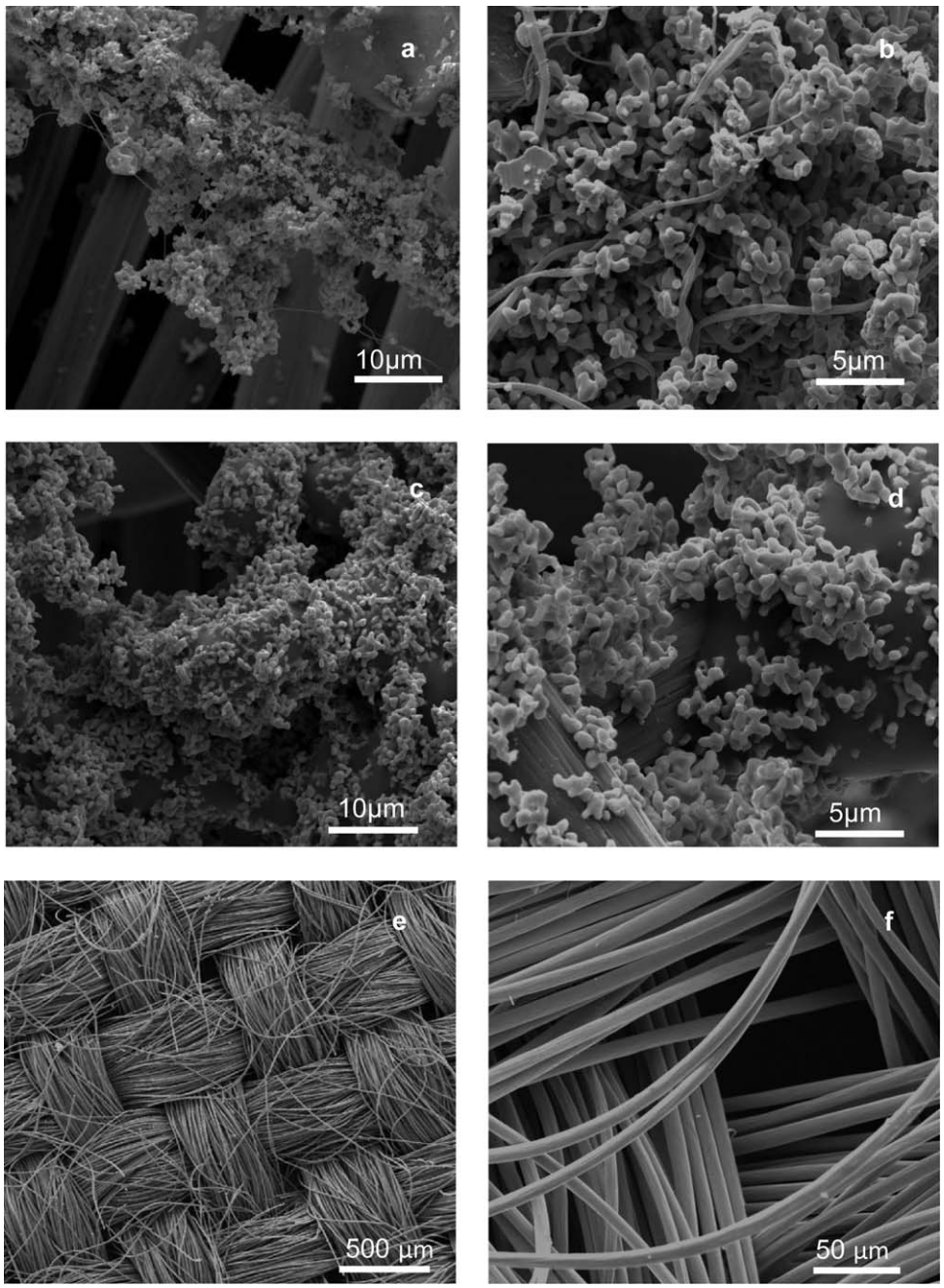

Figure 6. SEM images of E/E-ELAT 2 at (a) 5k X and (b) 10k X magnification and E/E-ELAT 2-A at (c) 5k X and (d) 10k X magnification and ELAT 2 at (e) 100 X and (f) 1k X magnification.

clearly. Additionally, the highly porous structure of the E/E-ELAT 1 membranes can be observed in Figure 5. Also, larger agglomerates or particles of PSU were observed (see lower left hand corner of SEM image in Figure 5a). During electrospinning, a polymer solution is ejected out of an electrified syringe needle resulting in Taylor cone at the tip and an elongated liquid jet that forms into nanofibers.[43] Occasionally during the electrospinning process, the polymer solution can clog at the needle tip due to the high viscosity of the solution resulting in a buildup of pressure. The needle was cleaned periodically during the electrospinning process to minimize clogging, but would quickly exit the needle as a spray and not a fiber directly after cleaning leading to a combination of PSU fibers and larger particles like those shown in Figures 5a, b. The 9.1 wt % PSU/DCM solution for electrospinning resulted in the highest number of PSU nanofibers. A solution concentration greater than 9.1 wt % PSU/DCM would lead to a membrane largely composed of PSU microfibers and large electrosprayed PSU particles, while a solution less than 9.1 wt % PSU/DCM would result in few PSU nanofibers and many electrosprayed PSU particles. Lowering the polymer solution concentration or viscosity results in no Taylor cone formation and thus primarily electrospraying instead of electrospinning.[43]

Figures 5c, d show SEM images of E/E membranes of electrospun PSU and electrosprayed Ti_4O_7 on ELAT 1 after the membranes were annealed at 200°C (E/E-ELAT 1-A). Larger PSU fibers are observed along with a fusing of Ti_4O_7 particles to the polymer and also to the ELAT 1. Figure 5d is a magnified view of the E/E-ELAT 1-A membrane shown in Figure 5c. The images show that the highly porous structure of the E/E-ELAT

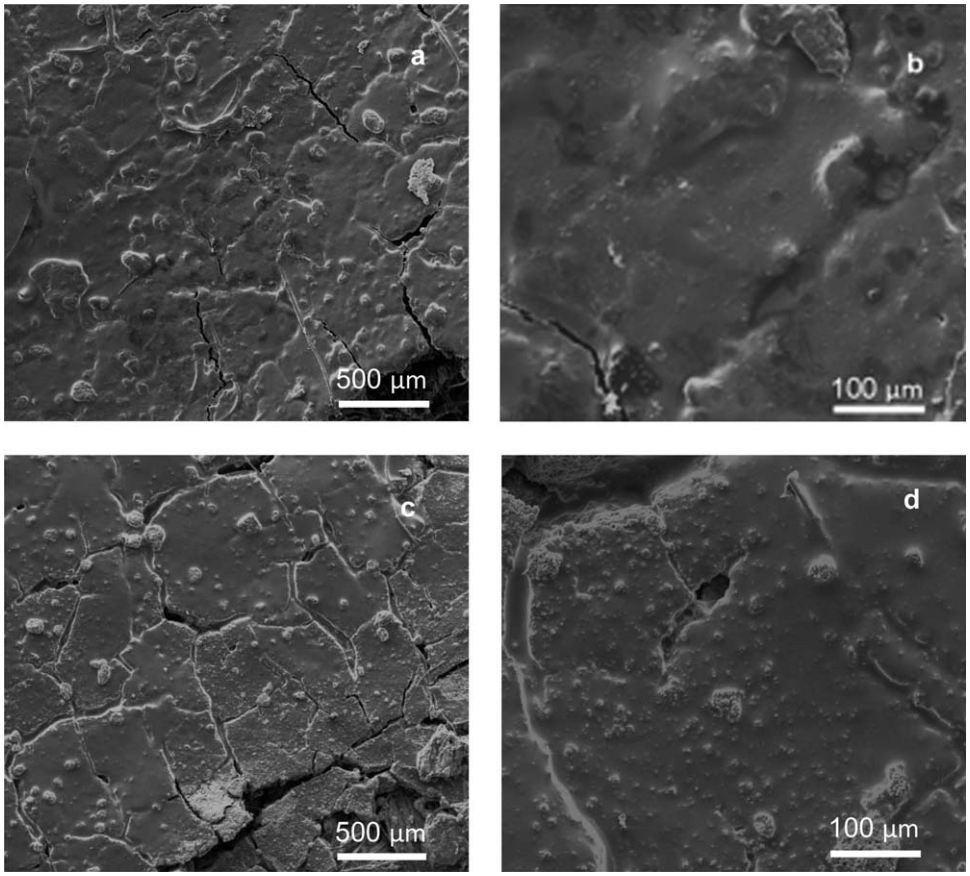

Figure 7. SEM images of SC-ELAT1 at (a) 100 X and (b) 500 X magnification and SC-ELAT 1-A at (c) 100 X and (d) 500 X magnification.

1-A membranes persists even after annealing. Therefore, annealing E/E-ELAT 1-A membranes results in highly porous, durable membranes with enhanced adhesion between materials that can subsequently be used for water filtration experiments.

Figures 5e, f show SEM images of the bare ELAT 1 used as the substrate for the E/E-ELAT 1 and E/E-ELAT 1-A membranes shown in Figures 5a–d. Figure 5e shows that the PTFE-treated microporous carbon layer on top of the woven carbon cloth membrane has a fairly uniform morphology across the substrate with visible cracks. Figure 5f shows a magnified view of Figure 5e, showing the morphology of the coating in more detail, highlighting the cracks in the coating, which are on the order of $\sim$10 μm.

Figures 6a, b show SEM images of E/E membranes of electrospun PSU and electrosprayed Ti_4O_7 on ELAT 2 before the membranes were annealed (E/E-ELAT 2). Figure 6b is a magnified view of the E/E-ELAT 2 membrane shown in Figure 6a, where both Ti_4O_7 particles and PSU nanofibers can be seen more clearly and the highly porous structure of the E/E PSU/Ti_4O_7 membranes can be observed. Similar to Figure 5, larger agglomerates, or particles of PSU were observed (see upper right hand corner of Figure 6a). Additionally, both Figures 5a, b and 6a, b display a network of micron-sized Ti_4O_7 particles and PSU nanofibers, demonstrating that regardless of the substrate, fabrication of a nanofiber/particle network occurs.

Figures 6c, d show SEM images of E/E membranes of electrospun PSU and electrosprayed Ti_4O_7 on ELAT 2 after the membranes were annealed at 200°C (E/E-ELAT 2-A). PSU fibers were not observed, but rather Ti_4O_7 particles fused to large agglomerates (melted fibers) of the polymer and also to the ELAT 2 was observed. Figure 6d is a magnified view of Figure 6c, where adhesion of the PSU and the Ti_4O_7 particles to the ELAT 2 large carbon fibers can be clearly seen. Similar to Figure 5, the images show that the E/E-ELAT 2-A membranes remain highly porous even after annealing, resulting in durable, highly porous membranes with enhanced adhesion between materials that can subsequently be used for water filtration experiments.

Figures 6e, f show SEM images of the bare ELAT 2 used as the substrate to create the E/E-ELAT 2 and E/E-ELAT 2-A membranes shown in Figures 6a–d. Figure 6e show that the ELAT 2 is comprised of a neatly woven carbon cloth membrane. Figure 6f shows a magnified view of Figure 6e clearly showing the carbon fibers and pores, which are on the order of $\sim$50 μm. The difference in pore size between ELAT 1 and ELAT 2 is due to the PTFE-treated microporous carbon layer present in ELAT 1. ELAT 2 is a bare woven carbon cloth membrane with a porosity of 80%. The PTFE-treated microporous carbon layer on ELAT 1 shown in Figures 5e, f completely covered the woven carbon cloth membrane reducing the porosity to 63%.

Solution cast membrane characterization

Figures 7a, b show SEM images of solution cast membranes of PSU/Ti_4O_7 on ELAT 1 before the membranes were annealed (SC-ELAT 1). Figure 7a shows a PSU/Ti_4O_7 film covering the PTFE-treated microporous carbon layer on the ELAT 1. Since there is only a PSU/Ti_4O_7 film covering the ELAT 1, the morphology in Figure 7a is similar to that of Figure 5e, showing the uniform morphology of the substrate with the PSU/Ti_4O_7 film sealing the cracks. Figure 7b is a

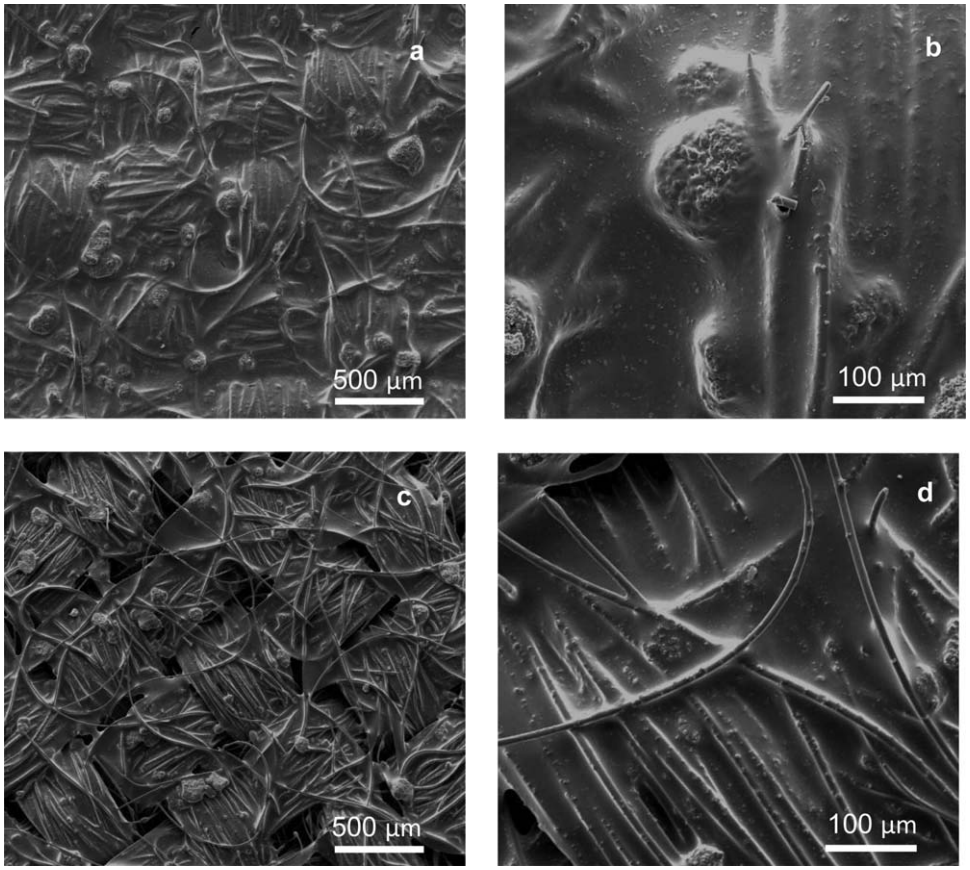

Figure 8. SEM images of SC-ELAT 2 at (a) 100 X and (b) 500 X magnification SC-ELAT 2-A and at (c) 100 X and (d) 500 X magnification.

magnified view of the solution cast membrane shown in Figure 6a showing the morphology of the film coating the ELAT 1 in detail, highlighting the Ti_4O_7 particles embedded in the PSU/Ti_4O_7 film. Figures 7c, d shows SEM images of solution cast membranes of PSU/Ti_4O_7 on ELAT 1 after the membranes were annealed at 200°C (SC-ELAT 1-A). Figure 7d is a magnified view of the solution cast membrane shown in Figure 7c. Since a PSU/Ti_4O_7 film was solution cast onto the ELAT 1, there is not a significant change in the PSU morphology shown in Figures 7c, d. The main difference is that Ti_4O_7 particles can be seen more clearly in Figures 7c, d than in Figures 7a, b. Unlike Figures 5 and 6, Figure 7 shows that the solution cast membranes do not have a highly porous structure because the PSU/Ti_4O_7 film covers the PTFE-treated microporous carbon layer on the ELAT 1 completely and creates a nonporous dense membrane film.

Figures 8a, b show SEM images of solution cast membranes of PSU/Ti_4O_7 on ELAT 2 before the membranes were annealed (SC-ELAT 2). Figure 8 shows a PSU/Ti_4O_7 film covering all the carbon fibers of the ELAT 2. Similar to Figure 7, the morphology in Figure 8b is a magnified view of the solution cast membrane shown in Figure 8a showing the morphology of the PSU/Ti_4O_7 film coating the ELAT 2 in detail, highlighting the Ti_4O_7 particles embedded in the PSU/Ti_4O_7 film. Figures 8c, d show SEM images of solution cast membranes of PSU/Ti_4O_7 on ELAT 2 after the membranes were annealed at 200°C (SC-ELAT 2-A). Figure 8d is a magnified view of the solution cast membrane shown in Figure 8c. Since a PSU/Ti_4O_7 film was solution cast onto the ELAT 2, there is not a significant change in the PSU morphology shown in Figures 8c, d. The main difference is that Ti_4O_7 particles can be seen more clearly in Figures 8c, d than in Figures 8a, b. Additionally, the annealed PSU film in Figure 8c shows gaps between the woven fibers that were not present in Figure 8a before the solution cast membranes were annealed. However, these appear to be a surface effect and not a pore that extends transverse through the membrane. Unlike Figures 5 and 6, but similar to Figure 7, Figure 8 shows that the solution cast membranes do not have a highly porous structure, but rather a nonporous dense membrane that covers the ELAT 2 substrate completely. The membranes in Figures 7 and 8 were fabricated merely as control membranes for comparison purposes and not with the expectation of achieving high reactivity during filtration experiments.

Electrical conductivity

Table 2 shows the electrical conductivity of the membranes. The solution cast membranes and bare ELAT 1 and ELAT 2

Table 2. Conductivity of Membranes

Sample Name	Conductivity (S/cm)
ELAT 1	47.25 ± 0.05
E/E-ELAT 1-A	45.67 ± 0.67
E/E-ELAT 1-A	41.35 ± 0.02
SC-ELAT 1-A	38.38 ± 0.13
ELAT 2	46.95 ± 0.07
E/E-ELAT 2-A	50.71 ± 0.07
E/E-ELAT 2-A	46.12 ± 0.05
E/E-ELAT 2-A-2	42.35 ± 0.54
SC-ELAT 2-A	42.18 ± 0.07

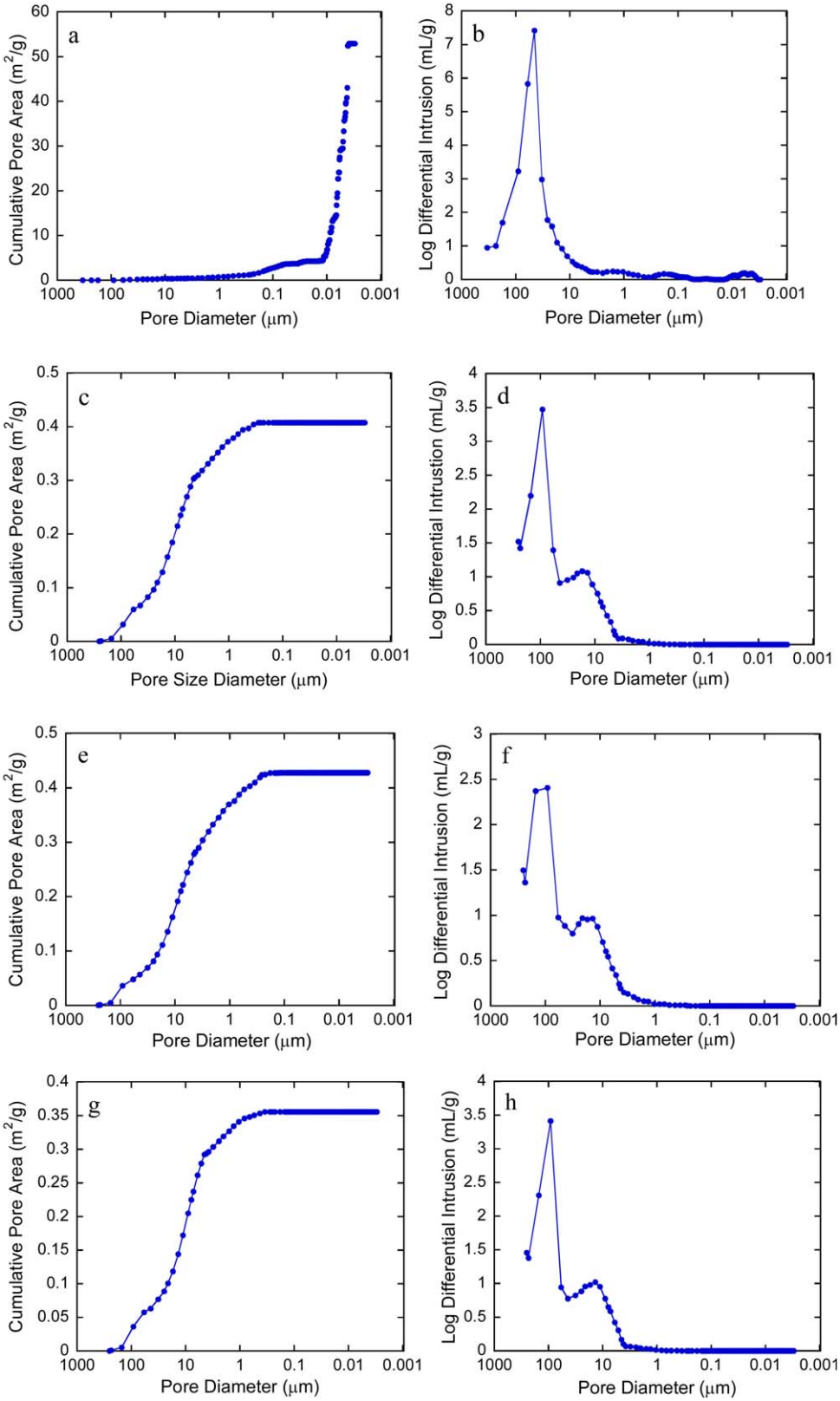

Figure 9. Results of Hg intrusion porosimetry analysis for (a,b) free-standing E/E membrane, (c,d) E/E-ELAT 2-A, (e,f) E/E ELAT 2-A-2, (g,h) ELAT 2. a,c,e,g refer to cumulative pore area and b,d,f,h refer to log differential intrusion pore volume (solid lines represent piece-wise linear interpolation).

[Color figure can be viewed in the online issue, which is available at wileyonlinelibrary.com.]

were tested as controls for the E/E membranes. The results in Table 2 show that the conductivity of ELAT 1 and ELAT 2 are similar in magnitude, demonstrating that the substrates used for creating the E/E and solution cast membranes were conductive. Additionally, the conductivities of the E/E and solution cast membranes are similar to those of bare ELAT 1

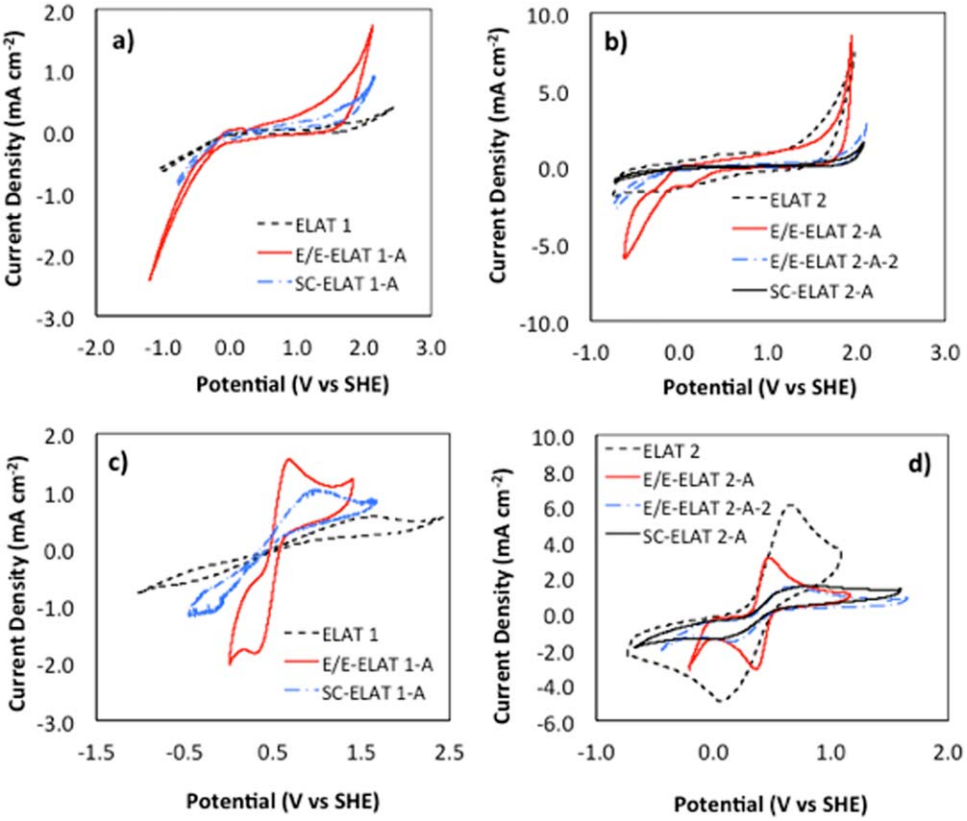

Figure 10. CV scans in 100 mM $NaClO_4$ supporting electrolyte for (a) ELAT 1 REMs and (b) ELAT 2 REMs. CV scans in 100 mM $NaClO_4$ supporting electrolyte and 5 mM $Fe(CN)_6^{4-/3-}$ redox couple for (c) ELAT 1 REMs and d) ELAT 2 REMs. Scan rate: 50 mV s^{-1}.

Experimental conditions: Working electrode = ELAT (10 cm^2); Counter electrode = Pt wire; Reference electrode = Ag/AgCl; T = 20°C; Scan rate: 50 mV s^{-1}. [Color figure can be viewed in the online issue, which is available at wileyonlinelibrary.com.]

and ELAT 2, indicating that the conductivities of the E/E and solution cast membranes are maintained. These results demonstrate that the E/E PSU/Ti_4O_7 membranes are not only highly porous and durable, but are also conductive, which is an important characteristic for REMs. Overall, these REMs are not resistant to electrical current and can subsequently be used for electrochemical water filtration experiments.

Hg porosimetery

The pore structure of the free-standing E/E membrane, E/E ELAT 2-A, E/E ELAT 2-A-2, and ELAT 2 were characterized using Hg intrusion porosimetry analysis. Figure 9 shows the cumulative pore area and the log differential intrusion as a function of the pore diameter for each membrane analyzed. Figure 9b shows that the majority of the pore volume of the free-standing E/E membrane consists of 16–45 μm sized pores. Unlike the free-standing E/E membrane, the composite membranes and bare ELAT 2 alone show different patterns for the cumulative pore area and the log differential intrusion. This is due to the ELAT 2 substrate (Figures 9g, h), which has a vastly different pore structure than the E/E PSU/Ti_4O_7 adhered to it. Figures 9d, f, h show significant peaks at approximately 15 μm and 100 μm. The 15 μm pore sizes are most likely due to the pores between the fibers of the bare ELAT 2 membrane, and the 100 μm pore sizes are most likely due to the pores between the bundles of fibers of the ELAT 2 membrane shown in Figures 6e, f.

Electrochemical characterization

The CV scans were used to characterize the potential window of water stability and the electrochemical response to the $Fe(CN)_6^{4-/3-}$ redox couple. This redox couple was chosen

Table 3. Summary of CV Data and Data Analysis for E/E REMs

Membrane Sample	I_{pa} (mA/cm^2)	I_{pc} (mA/cm^2)	I_{pa}/I_{pc}	ΔE_p (mV)	C_{dl} (F/cm^2)	$C_{dl,l}/C_{dl,ELAT2}$	ρ	$*k^\circ_{app}$ (cm/s)	k° (cm/s)†
ELAT 1	0.554	−0.570	0.97	2000	–	–	–	–	–
E/E-ELAT 1-A	1.55	−1.75	0.89	307	–	–	–	–	–
SC–ELAT 1-A	1.03	−1.04	0.99	1092	–	–	–	–	–
ELAT2	6.09	−4.92	1.24	583	3.37×10^{-4}	1.00	17	3.54×10^{-3}	2.10×10^{-4}
E/E ELAT 2-A	3.13	−2.92	1.07	77	1.32×10^{-4}	0.39	6.6	7.71×10^{-3}	1.17×10^{-3}
E/E ELAT 2-A-2	1.51	−1.65	0.92	454	3.56×10^{-5}	0.11	1.8	3.67×10^{-4}	2.07×10^{-4}
SC–ELAT 2-A	1.56	−1.45	1.08	782	1.03×10^{-4}	0.31	5.2	3.93×10^{-4}	7.64×10^{-5}

*= Determined by EIS measurements
†= Normalized by electroactive surface area determined by C_{dl} measurements (divided by ρ).

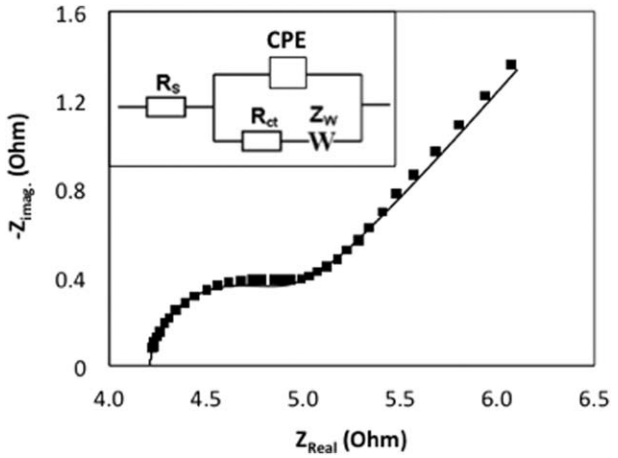

Figure 11. Electrochemical impedance spectra for E/E-ELAT 2-A over the frequency 0.4 Hz to 30 kHz in the presence of 5 mM $Fe(CN)_6^{4-/3-}$ redox couple in 100 mM $NaClO_4$ supporting electrolyte.

Experimental conditions: Working electrode = ELAT (10 cm^2); Counter electrode = Pt wire; Reference electrode = Ag/AgCl; T = 20°C.

because it undergoes a facile outer sphere electron transfer reaction and is used as a probe to assess the effect of Ti_4O_7 on the reaction kinetics toward the $Fe(CN)_6^{4-/3-}$ redox couple. Results of CV scans are shown in Figure 10.

Results in Figure 10a indicate that the ELAT 1 substrate had low activity for water oxidation and reduction reactions over the investigated potential range. By contrast, the E/E-ELAT 1-A sample showed an enhanced reactivity for both water oxidation and water reduction relative to ELAT 1, which was also much higher than for the solution cast REM (SC-ELAT 1-A). These results are attributed to the coating of the Ti_4O_7 particles by the PSU polymer, and the lower porosity created by the solution cast process relative to the E/E fabrication technique, which is evident from SEM images (Figures 5 and 7).

The CV scans for ELAT 2, E/E-ELAT 2-A, E/E-ELAT 2-A-2, and SC-ELAT 2-A are shown in Figure 10b. Results for the E/E-ELAT 2-A membrane showed that the addition of the Ti_4O_7 particles caused a slightly higher overpotential for water oxidation and lower overpotential for water reduction, which is characteristic of Ti_4O_7.[44] However, the results for both the E/E-ELAT 2-A-2 and SC-ELAT 2-A membranes indicate that water oxidation and reduction reactions were less active than on E/E-ELAT 2-A. These results are again attributed to the coating of the Ti_4O_7 particles by the PSU polymer, and the lower porosity (and thus surface area) created by the solution cast technique relative to the E/E fabrication technique, which is evident from SEM images (Figures 6 and 8). Additionally, it should be noted that the current density for water oxidation and reduction was much greater for the ELAT 2 materials (Figure 10b) relative to the ELAT 1 materials (Figure 10a), this result is attributed to the higher porosity of the ELAT 2 materials and the higher activity of ELAT 2 relative to ELAT 1 for water oxidation and reduction reactions, the latter is attributed to the hydrophobic PTFE-treated microporous carbon coating that is present on ELAT 1.

Investigation of the $Fe(CN)_6^{4-/3-}$ redox couple on the REMs is shown in Figures 10c, d and data summarizing the analysis of these CV curves is included in Table 3. For all CV scans with the $Fe(CN)_6^{4-/3-}$ redox couple, the anodic peak current (I_{pa}) to cathodic peak current (I_{pc}) ratio was close to unity ($I_{pa}/I_{pc} = 0.89 - 1.24$), indicating that neither homogeneous reactions nor adsorption were occurring during these scans.[45] The CV scans with the $Fe(CN)_6^{4-/3-}$ redox couple were used to determine changes to the reactive surface area and reaction kinetics of the $Fe(CN)_6^{4-/3-}$ redox couple. The reactive surface area was assessed by I_{pa} and reaction kinetics was qualitatively assessed by the anodic and cathodic peak separation (ΔE_p) (Table 3). The ELAT 1 substrate showed irreversible kinetics for the $Fe(CN)_6^{4-/3-}$ redox couple (Figure 10c), which was attributed to the hydrophobic PTFE-treated microporous carbon coating. The addition of the Ti_4O_7 particles by the E/E fabrication technique (E/E-ELAT 1-A) increased I_{pa} and decreased ΔE_p relative to ELAT, indicating an increase in the reaction surface area and enhancement of the reaction kinetics (Figure 10c and Table 3). SC-ELAT 1-A showed some enhancement of kinetics ($\Delta E_p = 1092$ mV) and reactive surface area ($I_{pa} = 1.03$ mA cm^{-2}) compared to the ELAT 1 substrate, but not to the extent of the E/E-ELAT 1-A membrane. The response was more irreversible than the E/E-ELAT 1-A, which was attributed to the coating of the Ti_4O_7 particles by the PSU polymer in the SC-ELAT 1-A membrane (see Figure 7).

CV scans in the presence of 5 mM $Fe(CN)_6^{4-/3-}$ redox couple for ELAT 2 REMs are shown in Figure 10d. The uncoated ELAT 2 substrate showed the highest peak current ($I_{pa} = 6.09$ mA cm^{-2}) and the largest peak separation ($\Delta E_p = 583$ mV) compared to the other ELAT 2 coated materials, except SC-ELAT 2-A (Table 3). On the addition of Ti_4O_7 to ELAT 2 by the E/E method (E/E-ELAT 2-A), it was observed that both ΔE_p and I_{pa} decreased (Figure 10d and Table 3). These results are once again attributed to the PSU polymer deposition on the ELAT 2 substrate. The E/E method operated under short deposition times (6 h) (E/E-ELAT 2-A) was able to deposit Ti_4O_7 particles with low PSU polymer coverage, that produced membranes with intimate contact between the Ti_4O_7 particles and the ELAT 2 porous matrix. By contrast, both the E/E method operated under extended deposition times

Table 4. Summary of Regressed Parameters from EIS Equivalent Circuit Model

Sample Name		R_s	R_{ct}	Y_o	A	W
ELAT 2	Value	4.76	1.48	3.13×10^{-2}	0.68	5.25×10^{-1}
	Error	0.07	0.27	1.63×10^{-2}	0.11	3.5×10^{-2}
E/E-ELAT 2-A	Value	4.22	0.68	1.98×10^{-2}	0.92	7.13×10^{-1}
	Error	0.06	0.21	7.92×10^{-3}	0.19	1.31×10^{-1}
E/E-ELAT 2-A-2	Value	2.75	14.23	2.52×10^{-3}	0.79	1.51×10^{-1}
	Error	0.02	0.39	1.64×10^{-4}	0.01	1.96×10^{-2}
SC-ELAT 2-A	Value	6.92	13.3	1.27×10^{-3}	0.71	2.89×10^{-1}
	Error	0.06	0.26	1.32×10^{-4}	0.02	2.77×10^{-2}

Errors represent 95% confidence intervals for fitted parameters.

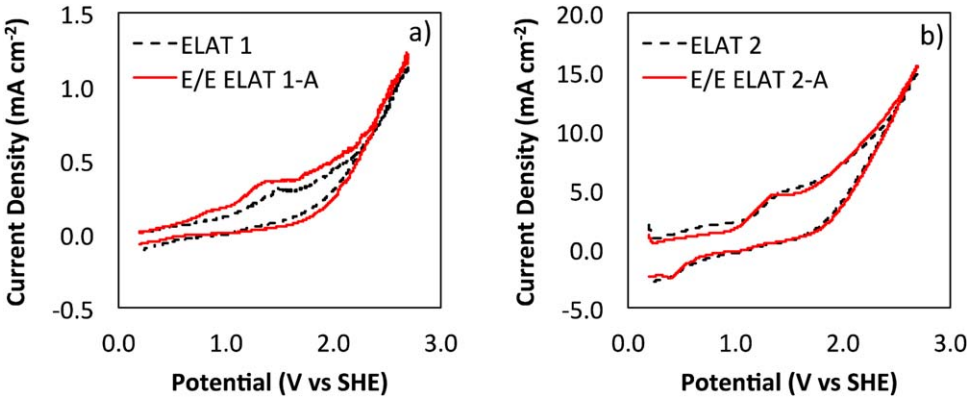

Figure 12. CV scans of 5 mM phenol in 100 mM $NaClO_4$ supporting electrolyte for (a) ELAT 1 and E/E ELAT 1-A and (b) ELAT 2 and E/E ELAT 2-A.

Experimental conditions: Working electrode = ELAT (10 cm^2); Counter electrode = Pt wire; Reference electrode = Ag/AgCl; T = 20°C; Scan rate: 50 mV s^{-1}. [Color figure can be viewed in the online issue, which is available at wileyonlinelibrary.com.]

(E/E-ELAT 2-A-2) and the solution cast method (SC-ELAT 2-A) produced membranes with excess PSU polymer coating that prevented access of aqueous solutes to the Ti_4O_7 particles and thus inhibited electron transfer rates. The SEM images in Figure 8 clearly show the coating of the Ti_4O_7 particles and the ELAT 2 substrate with the PSU polymer.

A more reversible reaction typically results in an increase in I_{pa}. The diminished I_{pa} observed after Ti_4O_7 addition (see Table 3) is attributed to reduction of the electroactive surface area during REM synthesis. The E/E-ELAT 2-A-2 membrane, which was subjected to the E/E process for 2 days, showed higher irreversibility than E/E-ELAT 2-A, which was synthesized for a shorter time (6 h). This result is attributed to an increase in PSU polymer deposition on the ELAT 2 substrate with E/E deposition time, which resulted in a decrease in the electroactive surface.

The ELAT 2-based REMs showed a higher reactivity for water oxidation and reduction and increased reversibility for the $Fe(CN)_6^{4-/3-}$ redox couple relative to the ELAT 1-based REMs. Therefore, ELAT 2-based REMs were chosen for further electrochemical characterization. The double layer capacitance (C_{dl}) values were measured for the ELAT 2-based REMs and were used to assess the change in electroactive surface area and to determine a roughness factor (ρ) for each of the REMs. Capacitance methods for the determination of electroactive surface area have been applied in prior studies.[46] The C_{dl} is a measure of the electroactive surface area of the materials and was highest for the bare ELAT 2 substrate ($C_{dl} = 3.37 \times 10^{-4}$ F cm^{-2}) and decreased after E/E and SC coatings. The ratio of $C_{dl,i}/C_{dl,ELAT\text{-}2}$ was 0.39, 0.11, and 0.31 for i = E/E-ELAT 2-A, E/E-ELAT 2-A-2, SC-ELAT 2-A, respectively. The values for $C_{dl,i}/C_{dl,ELAT\text{-}2}$ were similar to the $I_{pa,i}/I_{pa,ELAT\text{-}2}$ values determined from the CV data shown in Figure 10d, which were 0.51, 0.25, and 0.26 for i = E/E-ELAT 2-A, E/E-ELAT 2-A-2, and SC-ELAT 2-A, respectively. These results suggest that the deposition of the PSU/Ti_4O_7 decreased the electroactive surface area of the REMs, and this decrease in electro-active surface area was responsible for the decrease in I_{pa} observed in CV data (Figure 10d). The decrease in ΔE_p after the addition of Ti_4O_7 particles indicates that Ti_4O_7 was more active for the $Fe(CN)_6^{4-/3-}$ redox couple, than the bare ELAT 2 support.

The ρ value for each REM was estimated from the C_{dl} measurements by assuming an average double layer capacitance of 20 μF cm^{-2} for the bare ELAT 2 support.[47,48] The ρ for Ti_4O_7 coated samples was determined by assuming that the $C_{dl,i}/C_{dl,ELAT\text{-}2}$ ratio was representative of the change in surface area. This approach may overestimate the actual ρ values of the REMs, since the Ti_4O_7 particles likely have a slightly higher C_{dl} than the carbon support, but was deemed as a reasonable first order approximation. Results indicate that ELAT 2 had a ρ value of 17, and ρ decreased to 6.6, 1.8, and 5.2 for the E/E-ELAT 2-A, E/E-ELAT 2-A-2, and SC-ELAT 2-A REMs, respectively. The decrease in surface roughness is related to polymer deposition, which is apparent from SEM images. Figure 6 shows the deposition of large polymer deposits on the ELAT 2 coating when using the E/E deposition method, and Figure 8 shows a uniform coating when using the SC method.

EIS measurements were used to estimate the charge transfer resistance (R_{ct}) of the of 5 mM $Fe(CN)_6^{4-/3-}$ redox couple and to estimate a reaction rate constant. Figure 11 contains EIS data and an equivalent circuit model fit for the E/E-ELAT 2-A REM. A summary of all the regressed parameters from the equivalent circuit model fits of all the ELAT 2-based REMs are shown in Table 4. The EIS results support the results obtained from the CV data. The apparent standard heterogeneous rate constant (k^o_{app}) was determined for the tested redox couple using the measured value of R_{ct} and the following equation[45]

$$k^{\circ}_{app} = \frac{RT}{R_{ct}ACF^2} \tag{6}$$

where R is the ideal gas constant, T is temperature, C is the concentration of the redox couple, A is the membrane geometric surface area, and F is Faraday's constant. The standard rate constant (k^o) was also estimated by dividing by the roughness factor to normalize by the "real" electroactive surface area. Results are shown in Table 3. The comparable k^o values show that the difference in CV curves for ELAT 2 and E/E-ELAT 2-A-2 are attributed to surface area changes, and also that the C_{dl} ratio is an accurate approximation of the change in electroactive surface area. The E/E-ELAT 2-A material showed changes to reversible behavior, which increased the surface area normalized rate constant (k^o) by a factor of > 5, which is attributed to enhanced kinetics on Ti_4O_7 particles relative to the ELAT 2 support.

Overall the results from CV and EIS analyses indicate that the ELAT 2 substrate was more active for water electrolysis

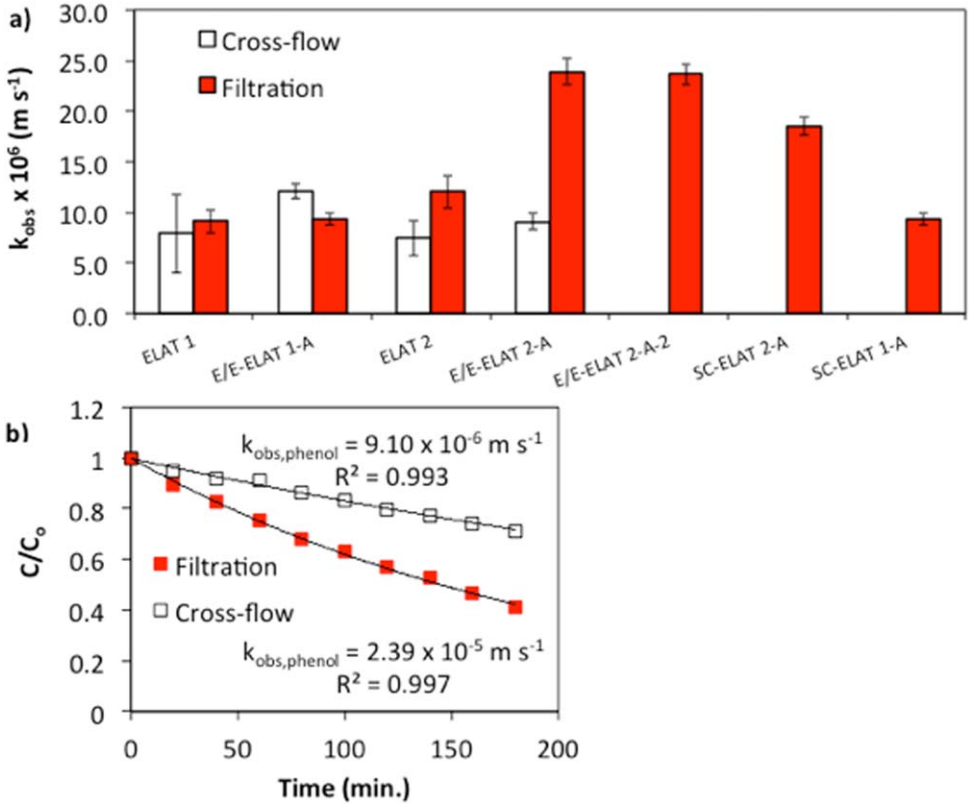

Figure 13. (a) Summary of phenol oxidation rate constants, (b) data of phenol vs. time for E/E-ELAT 2-A. Solid lines represent model fits. All experiments conducted at 1.0 mA cm^{-2} current density.

Cross-flow mode experiments were not conducted for E/E-ELAT 2-A-2, SC-ELAT 2-A, and SC-ELAT 1-A. Error bars represent 95% confidence intervals on regressed k_{obs} values obtained from experiments on duplicate samples for each REM. Experimental conditions: Anode = ELAT (10 cm^2); Cathode = BDD (10 cm^2); electrolyte: 0.3 L of 100 mM KH_2PO_4; T = 20°C; Q_{cross} = 25.8 L h^{-1}; J = 6100 L m^{-2} h^{-1}. [Color figure can be viewed in the online issue, which is available at wileyonlinelibrary.com.]

reactions and reaction with the $Fe(CN)_6^{4-/3-}$ redox couple relative to ELAT 1, which was attributed to the hydrophobic PTFE-treated microporous carbon coating on ELAT 1 that was less active for these reactions and also acted to reduce the total surface area (per SEM images). It also was found that the deposition of the Ti_4O_7 particles by the E/E method for 6 h (E/E-ELAT 2-A) produced the best membranes with respect to increased activity for water electrolysis and the $Fe(CN)_6^{4-/3-}$ redox couple. The response was highly correlated to the content of PSU polymer on the REM material, which acted to reduce the electroactive surface area for the E/E-ELAT 2-A-2 and SC-ELAT 2-A membranes.

Flow-through experiments

To determine the potential of the E/E REMs for water treatment applications, a series of experiments were conducted to assess phenol oxidation. CV scans were first conducted in batch mode to assess the direct oxidation of phenol (Figure 12). Peaks associated with the direct oxidation of phenol ($E \sim$ 1.3 V) indicate some enhancement for E/E-ELAT 1-A relative to ELAT 1 (Figure 12a), and results were similar for both E/E-ELAT 2-A and ELAT 2 (Figure 12b). Direct oxidation of phenol was much greater on the ELAT 2 materials compared to the ELAT 1 materials, which is consistent with results shown in Figure 10. To assess bulk phenol oxidation by both direct oxidation and reaction with $OH^{\bullet}$, the E/E REMs were tested in the flow-through reactor shown in Figure 2. Experiments were conducted in both cross-flow and filtration mode, and for both

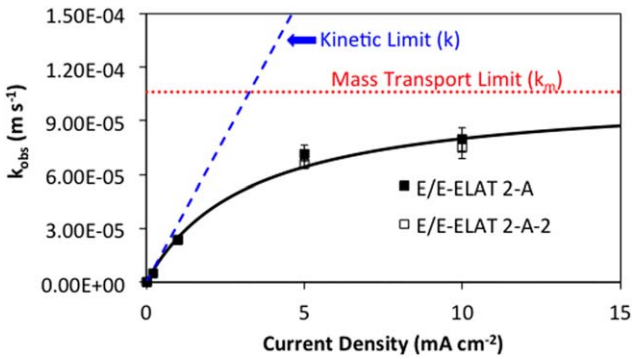

Figure 14. Plot of normalized observed rate constant (k_{obs}) for phenol oxidation in the flow-through reactor operated in filtration mode as a function of current density.

Solid black line—model fit (Eq. 7); Blue dashed line—kinetic limit estimated by model fit to experimental data; red dashed line—mass transport limit (k_m) estimated by model fit to experimental data. Error bars represent 95% confidence intervals on regressed k_{obs} values obtained from experiments on duplicate samples for each REM. Experimental conditions: Anode = ELAT (10 cm^2); Cathode = BDD (10 cm^2); electrolyte: 0.3 L of 100 mM KH_2PO_4; T = 20°C; Q_{cross} = 25.8 L h^{-1}; J = 6100 L m^{-2} h^{-1}. [Color figure can be viewed in the online issue, which is available at wileyonlinelibrary.com.]

flow configurations the cross-flow rate was held constant ($Q = 25.8$ L h^{-1}) and solutions were 100% recycled to the feed reservoir to characterize removal kinetics. Results for phenol oxidation experiments at a current density of 1.0 mA cm^{-2} are shown in Figure 13a. The kinetics for phenol removal were found to be first-order, and an example of the data and the first-order model fit (k_{obs}) are provided in Figure 13b. Extensive product formation was not characterized, but results from chemical oxygen demand (COD) data indicate only a modest removal of COD (~10–20%), which indicates that phenol was oxidized to other products and neither substantial polymerization nor mineralization of phenol occurred. When the REMs were operated in filtration mode vs. cross-flow mode, the k_{obs} for phenol removal changed by a factor of 1.2, 0.8, and 1.6 for the ELAT 1, E/E-ELAT 1-A, and ELAT 2 REMs, respectively (Figure 12a). The lack of a significant change between filtration and cross-flow operation indicates that reaction kinetics were not significantly affected by mass transport and were at or near the kinetic limit. We expected an enhancement in reaction kinetics for E/E ELAT 1, but k_{obs} was similar to ELAT 1. It, therefore, is possible that the dense ELAT 1 substrate, which contained the PTFE treated microporous carbon layer, created preferential flow paths, and the Ti_4O_7 particles were bypassed during filtration. However, when the E/E-ELAT 2-A REM was operated in filtration mode, the k_{obs} for phenol increased by a factor of 2.6 compared to cross-flow mode experiments. These results are attributed to a significant enhancement of the mass-transfer rate of phenol to the REM surface, which thereby allowed the enhanced kinetics of phenol oxidation on the Ti_4O_7 particles to be realized. These results indicate that mass transfer in the cross-flow mode limited the k_{obs} and that filtration mode through a highly porous REM is necessary to realize the high reactivity of these materials. The E/E-ELAT 2-A-2 showed similar kinetics to the E/E-ELAT 2-A, suggesting some mass transport control existed and the change in electroactive surface area between the two materials cited prior did not significantly affect kinetics. By contrast, the SC-ELAT 2-A showed a lower rate constant for phenol ($k_{obs} = 1.85 \times 10^{-5} \pm 9.10 \times 10^{-7}$ m s^{-1}) compared to the E/E-ELAT 2-A REM ($k_{obs} = 2.39 \times 10^{-5} \pm 1.35 \times 10^{-6}$ m s^{-1}), which is consistent with the CV and EIS results that showed slower kinetics for the $Fe(CN)_6^{4-/3-}$ redox couple (Table 3). Results also indicate that the ELAT 2 materials performed better than the ELAT 1 materials when operated in filtration mode, which is attributed to enhanced kinetics on ELAT 2 materials, similar to CV results with the $Fe(CN)_6^{4-/3-}$ redox couple.

Based on the results that indicate the ELAT 2 materials had faster kinetics for the $Fe(CN)_6^{4-/3-}$ redox couple and phenol oxidation relative to the ELAT 1 materials, additional filtration mode experiments were conducted to determine the effect of current density on phenol oxidation for the ELAT 2 materials. A series of experiments were conducted at various current densities (i.e., 0.2–10 mA cm^{-2}) using the ELAT 2-based REM materials (Figure 14). The k_{obs} values determined for phenol oxidation were fit with the following equation

$$k_{obs} = \frac{k_m}{1 + \frac{k_m}{k}} \quad (7)$$

$$k = \frac{i}{nFAC_0}\gamma \quad (8)$$

where k_{obs} is the normalized observed first-order reaction rate constant (m s^{-1}), k_m is the normalized mass-transport rate constant (m s^{-1}), k is the normalized kinetic rate constant (m s^{-1}), C_0 is the initial phenol concentration (mol m^{-3}), and γ is the fraction of current going toward phenol oxidation. Equation 8 implies that the kinetic rate constant increases linearly with the applied current, which has been observed in prior electrochemical studies.[49,50] All other symbols have their usual meanings. Equation 7 was fit to the k_{obs} data using least squares regression, where $\gamma = 0.31$ and $k_m = 1.1 \times 10^{-4}$ m s^{-1} were the best-fit parameter values. As shown in Figure 14, the model adequately represents the data, and indicates that k_{obs} for phenol oxidation at 10 mA cm^{-2} for E/E-ELAT 2-A ($k_{obs} = 8.0 \times 10^{-5}$ m s^{-1}) and E/E-ELAT 2-A-2 ($k_{obs} = 7.5 \times 10^{-5}$ m s^{-1}) were approaching the mass transfer limit. The k_{obs} values for phenol oxidation measured here are 6 to 8 times higher than measured in a previous study that utilized a ceramic Ti_4O_7 REM operated in filtration mode for *p*-substituted phenol oxidation ($k_m = 1.0 \times 10^{-5}$ to 1.4×10^{-5} m s^{-1}),[1,2] and is comparable to rate constants obtained with carbon nanotube flow-through reactors (1.7×10^{-5} to 1.0×10^{-4} m s^{-1}), which are among the highest reported in the literature.[51–53]

Previous work with a ceramic Ti_4O_7 REM operated in filtration mode showed that the rate constants for oxidation of various organic compounds were convection-limited due to the ~1.0 micron pore size.[1] Fitting of the k_{obs} values in our experiments with Eq. 7 determined that $k_m = 1.1 \times 10^{-4}$ m s^{-1}. The normalized membrane flux (J) through the REM was 1.7×10^{-3} m s^{-1} (6100 L m^{-2} h^{-1}), which is an order of magnitude higher than the value determined for k_m. These results suggest that phenol oxidation was limited by pore diffusion within the REM and not convection to the pore. The diffusion length (δ) was estimated by $\delta = D/k_m$, where D is the diffusion coefficient for phenol ($D = 8.9 \times 10^{-10}$ m^2 s^{-1}).[54] Based on $k_m = 1.1 \times 10^{-4}$ m s^{-1}, a value of $\delta = 8.4$ μm was estimated. The Hg porosimetry data (see Figure 9) indicated that the ELAT 2 support has pores on the order of 15 μm. The value of $\delta = 8.4$ μm is almost identical to the average pore radius of 7.5 μm found by Hg porosimetry, and indicates the pore diffusion was controlling phenol oxidation. Additionally, these results indicate that designing REM materials with smaller pore diameters should result in enhanced removal of contaminants.

Conclusions

This study synthesized porous, flexible REMs by a novel simultaneous E/E technique for use in water treatment applications. REMs consisted of PSU fibers and Ti_4O_7 particles, supported on an ELAT gas diffusion layer substrate. SEM images of annealed samples showed that the synthesized REMs consisted of well-adhered micron-sized Ti_4O_7 particles to the ELAT substrate. Deposition of the Ti_4O_7 particles using the E/E technique resulted in an enhancement of the kinetics for water electrolysis reactions and the $Fe(CN)_6^{4-/3-}$ redox couple. By contrast, membranes synthesized by a solution cast method did not show kinetic enhancements for these reactions, which was attributed to PSU coverage of the Ti_4O_7 particles. Electrochemical impedance spectroscopy of the optimized REM measured a > 5-fold increase in the surface area normalized rate constant for the $Fe(CN)_6^{4-/3-}$ redox couple relative to the ELAT support. Membrane filtration experiments showed that operating the REMs in filtration mode resulted in a 2.6-fold enhancement in the observed first-order rate constant for phenol oxidation ($k_{obs,phenol}$) relative to cross-flow operation at a current density of 1.0 mA cm^{-2}. This enhancement was attributed to the increased mass transfer rate that

occurred in filtration mode. Phenol oxidation in filtration mode reached a $k_{obs,phenol} = 8.0 \times 10^{-5}$ m s^{-1} at 10 mA cm^{-2}, which was approaching the pore diffusion mass transfer limit, and was 6 to 8 times higher than measured in a previous study that utilized a ceramic Ti_4O_7 REM in filtration mode,[1,2] and is comparable to rate constants obtained with carbon nanotube flow-through reactors (1.7×10^{-5} to 1.0×10^{-4} m s^{-1}), which are among the highest reported in the literature to date.[51–53] Results suggest that further rate enhancements can be achieved by synthesizing REMs with smaller pore diameters, which will decrease the time-scale for pore diffusion.

Acknowledgments

The authors acknowledge the financial support of the National Science Foundation (CBET-1447172 and CBET-1356031) and for use of the SEM, which was acquired with support by the National Science Foundation (DBI-0116835), Texas A&M University, and the Texas Engineering Experimental Station.

Literature Cited

1. Zaky AM, Chaplin BP. Porous substoichiometric TiO2 anodes as reactive electrochemical membranes for water treatment. *Environ Sci Technol*. 2013;47(12):6554–6563.
2. Zaky AM, Chaplin BP. Mechanism of P-substituted phenol oxidation at a Ti_4O_7 reactive electrochemical membrane. *Environ Sci Technol*. 2014;48(10):5857–5867.
3. Hayfield PCS. *Development of a New Material - Monolithic Ti_4O_7 Ebonex® Ceramic*. Cambridge, UK: Royal Society of Chemistry, 2002.
4. Senevirathne K, Hui R, Campbell S, Ye SY, Zhang JJ. Electrocatalytic activity and durability of Pt/NbO2 and Pt/Ti_4O_7 nanofibers for pem fuel cell oxygen reduction reaction. *Electrochim Acta*. 2012;59: 538–547.
5. Pollock RJ, Houlihan JF, Bain AN, Coryea BS. Electrochemical Properties of a New Electrode Material, Ti_4O_7. *Mater Res Bull*. 1984;19(1):17–24.
6. Li XX, Zhu AL, Qu W, Wang HJ, Hui R, Zhang L, Zhang JJ. Magneli phase Ti_4O_7 electrode for oxygen reduction reaction and its implication for zinc-air rechargeable batteries. *Electrochim Acta*. 2010;55(20):5891–5898.
7. Kao WH, Patel P, Haberichter SL. Formation enhancement of a lead/acid battery positive plate by Barium Metaplumbate and Ebonex. *J Electrochem Soc*. 1997;144(8):2942–2942.
8. Loyns AC, Hill A, Ellis KG, Partington TJ, Hill JM. Bipolar batteries based on Ebonex® technology. *J Power Sources*. 2005;144(2): 329–337.
9. Chen GY, Bare SR, Mallouk TE. Development of supported bifunctional electrocatalysts for unitized regenerative fuel cells. *J Electrochem Soc*. 2002;149(8):A1092–A1099.
10. Ioroi T, Senoh H, Yamazaki SI, Siroma Z, Fujiwara N, Yasuda K. Stability of corrosion-resistant magneli-phase Ti_4O_7-supported pemfc catalysts at high potentials. *J Electrochem Soc*. 2008;155(4):B321–B326.
11. Phillips R, Hansen P, Eisenbraun E. Atomic layer deposition fabricated substoichiometric TiOx nanorods as fuel cell catalyst supports. *J Vac Sci Technol. A*. 2012;30(1):6.
12. Chen G, Betterton EA, Arnold RG. Electrolytic oxidation of trichloroethylene using a ceramic anode. *J Appl Electrochem*. 1999;29(8): 961–970.
13. El-Sherif S, Bejan D, Bunce NJ. Electrochemical oxidation of sulfide ion in synthetic sour brines using periodic polarity reversal at Ebonex® electrodes. *Can J Chem*. 2010;88(9):928–936.
14. Kearney D, Bejan D, Bunce NJ. The use of Ebonex electrodes for the electrochemical removal of nitrate ion from water. *Can J Chem*. 2012;90(8):666–674.
15. Bejan D, Malcolm JD, Morrison L, Bunce NJ. Mechanistic investigation of the conductive ceramic Ebonex® as an anode material. *Electrochim Acta*. 2009;54(23):5548–5556.
16. Bejan D, Guinea E, Bunce NJ. On the nature of the hydroxyl radicals produced at boron-doped diamond and Ebonex® anodes. *Electrochim Acta*. 2012;69:275–281.
17. Scialdone O, Galia A, Filardo G. Electrochemical incineration of 1,2-dichloroethane: effect of the electrode material. *Electrochim Acta*. 2008;53(24):7220–7225.
18. Wang X, Richey FW, Wujcik KH, Elabd YA. Ultra-low platinum loadings in polymer electrolyte membrane fuel cell electrodes fabricated via simultaneous electrospinning/electrospraying method. *J Power Sources*. 2014;264:42–48.
19. Yanilmaz M, Lu Y, Dirican M, Fu K, Zhang XW. Nanoparticle-on-nanofiber hybrid membrane separators for lithium-ion batteries via combining electrospraying and electrospinning techniques. *J Membr Sci*. 2014;456:57–65.
20. Wang K, Xu M, Zhu M, Su H, Wang H, Kong D, Wang L. Creation of macropores in electrospun silk fibroin scaffolds using sacrificial peo-microparticles to enhance cellular infiltration. *J Biomed Mater Res A*. 2013;101(12):3474–3481.
21. Virovska D, Paneva D, Manolova N, Rashkov I, Karashanova D. Electrospinning/electrospraying vs. electrospinning: a comparative study on the design of poly(L-lactide)/zinc oxide non-woven textile. *Appl Surf Sci*. 2014;311:842–850.
22. Thayer PS, Dimling AF, Plessl DS, Hahn MR, Guelcher SA, Dahlgren LA, Goldstein AS. Cellularized cylindrical fiber/hydrogel composites for ligament tissue engineering. *Biomacromolecules*. 2014;15(1):75–83.
23. Ignatova M, Manolova N, Rashkov I. Electrospun antibacterial chitosan-based fibers. *Macromol Biosci*. 2013;13(7):860–872.
24. Bock N, Woodruff MA, Steck R, Hutmacher DW, Farrugia BL, Dargaville TR. Composites for delivery of therapeutics: combining melt electrospun scaffolds with loaded electrosprayed microparticles. *Macromol Biosci*. 2014;14(2):202–214.
25. Bae H, Lee J. Encapsulated particles attached on electrospun fibers by in situ combination of electrospinning and coaxial electrospraying. *J Nanosci Nanotechnol*. 2014;14(10):7574–7580.
26. Wang X, Richey FW, Wujcik KH, Ventura R, Mattson K, Elabd YA. Effect of polytetrafluoroethylene on ultra-low platinum loaded electrospun/electrosprayed electrodes in proton exchange membrane fuel cells. *Electrochim Acta*. 2014;139:217–224.
27. Lavielle N, Hebraud A, Schlatter G, Thony-Meyer L, Rossi RM, Popa AM. Simultaneous electrospinning and electrospraying: a straightforward approach for fabricating hierarchically structured composite membranes. *ACS Appl Mater Interfaces*. 2013;5(20): 10090–10097.
28. Korina E, Stoilova O, Manolova N, Rashkov I. Poly(3-hydroxybutyrate)-based hybrid materials with photocatalytic and magnetic properties prepared by electrospinning and electrospraying. *J Mater Sci*. 2014;49(5):2144–2153.
29. Ding YC, Wu Q, Zhao D, Ye W, Hanif M, Hou HQ. Flexible Pi/BaTiO3 dielectric nanocomposite fabricated by combining electrospinning and electrospraying. *Eur Polym J*. 2013;49(9):2567–2571.
30. Lombardi M, Palmero P, Sangermano M, Varesano A. Electrospun polyamide-6 membranes containing titanium dioxide as photocatalyst. *Polym Int*. 2011;60(2):234–239.
31. An S, Lee MW, Joshi BN, Jo A, Jung J, Yoon SS. Water purification and toxicity control of chlorophenols by 3D nanofiber membranes decorated with photocatalytic titania nanoparticles. *Ceram Int*. 2014;40(2):3305–3313.
32. Roso M, Sundarrajan S, Pliszka D, Ramakrishna S, Modesti M. Multifunctional membranes based on spinning technologies: the synergy of nanofibers and nanoparticles. *Nanotechnology*. 2008;19(28): 285707.
33. Nabe A, Staude E, Belfort G. Surface Modification of Polysulfone Ultrafiltration Membranes and Fouling by Bsa Solutions. *J Membr Sci*. 1997;133(1):57–72.
34. Zodrow K, Brunet L, Mahendra S, Li D, Zhang A, Li Q, Alvarez PJJ. Polysulfone ultrafiltration membranes impregnated with silver nanoparticles show improved biofouling resistance and virus removal. *Water Res*. 2009;43(3):715–723.
35. Chakrabarty B, Ghoshal AK, Purkait MK. Ultrafiltration of stable oil-in-water emulsion by polysulfone membrane. *J Membr Sci*. 2008; 325(1):427–437.
36. Lima AA, Montalvao AF, Dezotti M, Sant'Anna GL. Ozonation of a complex industrial effluent: oxidation of organic pollutants and removal of toxicity. *Ozone Sci Eng*. 2006;28(1):3–8.
37. Li G, An T, Chen J, Sheng G, Fu J, Chen F, Zhang S, Zhao H. Photoelectrocatalytic decontamination of oilfield produced wastewater containing refractory organic pollutants in the presence of high concentration of chloride ions. *J Hazard Mater*. 2006;138(2):392–400.

38. Westerhoff P, Moon H, Minakata D, Crittenden J. Oxidation of organics in retentates from reverse osmosis wastewater reuse facilities. *Water Res*. 2009;43(16):3992–3998.
39. Buxton GV, Greenstock CL, Helman WP, Ross AB. Critical-review of rate constants for reactions of hydrated electrons, hydrogen-atoms and hydroxyl radicals (.Oh/.O-) in aqueous-solution. *J Phys Chem Ref Data*. 1988;17(2):513–886.
40. Goldschmidt D, Watanabe M. X-ray-diffraction of polycrystalline Ti_4O_7. *Mater Res Bull*. 1985;20(1):65–70.
41. Andersson S, Jahnberg L. Crystal structure studies on homologous series Ti_nO_{2n-1} V_nO_{2n-1} and Ti_{n-2} Cr_2O_{2n-1}. *Arkiv for Kemi*. 1964;21(5):413.
42. Lepage Y, Strobel P. Structural chemistry of magneli phases Ti_nO_{2n-1} ($4 \leq n \leq 9$) .1. Cell and structure comparisons. *J Solid State Chem*. 1982;43(3):314–319.
43. Li D, Xia Y. Electrospinning of nanofibers: reinventing the wheel? *Adv Mater*. 2004;16(14):1151–1170.
44. Walsh FC, Wills RGA. The continuing development of magneli phase titanium sub-oxides and Ebonex (R) electrodes. *Electrochim Acta*. 2010;55(22):6342–6351.
45. Bard AJ, Faulkner LR. *Electrochemical Methods: Fundamentals and Applications*. 2nd ed. New York, NY: Wiley, 2000.
46. Tremblay ML, Martin MH, Lebouin C, Lasia A, Guay D. Determination of the real surface area of powdered materials in cavity microelectrodes by electrochemical impedance spectroscopy. *Electrochima Acta*. 2010;55(21):6283–6291.
47. Shi H. Activated carbons and double layer capacitance. *Electrochim Acta*. 1996;41(10):1633–1639.
48. Frackowiak E, Beguin F. Carbon materials for the electrochemical storage of energy in capacitors. *Carbon*. 2001;39(6):937–950.
49. Canizares P, Garcia-Gomez J, Lobato J, Rodrigo MA. Modeling of wastewater electro-oxidation processes part I. General description and application to inactive electrodes. *Ind Eng Chem Res*. 2004;43(9):1915–1922.
50. Chaplin BP, Schrader G, Farrell J. Electrochemical destruction of N-nitrosodimethylamine in reverse osmosis concentrates using boron-doped diamond film electrodes. *Environ Sci Technol*. 2010;44(11):4264–4269.
51. Yang J, Wang J, Jia JP. Improvement of electrochemical wastewater treatment through mass transfer in a seepage carbon nanotube electrode reactor. *Environ Sci Technol*. 2009;43(10):3796–3802.
52. Tsierkezos NG, Ritter U. Electrochemical and thermodynamic properties of hexacyanoferrate(II)/(III) redox system on multi-walled carbon nanotubes. *J Chem Thermodyn*. 2012;54:35–40.
53. Schnoor MH, Vecitis CD. Quantitative examination of aqueous ferrocyanide oxidation in a carbon nanotube electrochemical filter: effects of flow rate, ionic strength, and cathode material. *J Phys Chem C*. 2013;117(6):2855–2867.
54. Haynes WM. *CRC Handbook of Chemistry and Physics*, *91st ed*. Boca Raton, FL: Taylor & Francis, 2010.

Manuscript received July 1, 2015, and revision received Sep. 28, 2015.